



A self-sufficient pressure pump using latex balloons for microfluidic applications

Journal:	<i>Lab on a Chip</i>
Manuscript ID	LC-ART-05-2018-000471.R1
Article Type:	Paper
Date Submitted by the Author:	17-Jul-2018
Complete List of Authors:	Thurgood, Peter; RMIT University, School of Engineering Zhu, Jiu; RMIT University, School of Electrical and Computer Engineering Nguyen, Ngan; RMIT University, School of Engineering Nahavandi, Saeid; Deakin University, Centre for Intelligent Systems Research Jex, Aaron; Walter and Eliza Hall Institute of Medical Research Pirogova, Elena; RMIT University, School of Engineering Baratchi, Sara; RMIT University, Khoshmanesh, Khashayar; RMIT University, School of Engineering

A self-sufficient pressure pump using latex balloons for microfluidic applications

Peter Thurgood ^{1,†}, Jiu Yang Zhu ¹, Ngan Nguyen ¹, Saeid Nahavandi ², Aaron R. Jex ^{3,4},
Elena Pirogova ¹, Sara Baratchi ⁵, Khashayar Khoshmanesh ^{1,†}

¹ School of Engineering, RMIT University, Melbourne, Australia

² Institute for Intelligent Systems Research and Innovation, Deakin University, Waurn Ponds,
Australia

³ Population Health and Immunity Division, The Walter and Eliza Hall Institute of Medical
Research, Parkville, Australia

⁴ Faculty of Veterinary and Agricultural Sciences, The University of Melbourne, Parkville,
Australia

⁵ School of Health and Biomedical Sciences, RMIT University, Bundoora, Australia

† Corresponding authors:

Peter Thurgood: pthurgood@gmail.com

Khashayar Khoshmanesh: Khashayar.khoshmanesh@rmit.edu.au

Abstract:

Here, we demonstrate a self-sufficient, inexpensive and disposable pressure pump using commercially available latex balloons. The versatility of the pump is demonstrated against various microfluidic structures, liquid viscosities, and ambient temperatures. The flow rate of the pump can be controlled by varying the size and thickness of the balloon. Importantly, the soft structure of the balloon allows for almost instantaneous change of flow rate upon manual squeezing of the balloon. This feature has been used for dynamically changing the flow ratio of parallel streams in a T-shaped channel or varying the size of droplets in a droplet generation system. The self-sufficiency, simplicity of fabrication and operation, along with the low-cost of the balloon pump facilitates the widespread application of microfluidic technologies for various research, education, and *in-situ* monitoring purposes.

Introduction

Pumping is essential for driving liquids through flow-through microfluidic systems. Pumping mechanisms can be categorised into three major groups, including passive, manually operated, and active pumps¹⁻³. Passive mechanisms rely on natural effects to drive liquid through microfluidic structures. The most common passive mechanism is the capillary effect, which relies on the cohesion between liquid molecules and the adhesion forces between the liquid and the microfluidic structure to drive flow^{4, 5}. Despite their simplicity, the flow rates of such passive mechanisms are relatively low and can only be provided for a short amount of time, in the order of a few minutes. Also, the flow rate depends on the geometry of the microfluidic structure and cannot be controlled, limiting its utility to simple, single-step assays^{6, 7}. Alternatively, manually operated pumping mechanisms can be simply provided by actuating a syringe⁸⁻¹⁰, a blister pouch^{11, 12}, a pressure chamber¹³⁻¹⁵, hand-crank¹⁶ or even spinning of a disc to produce sufficient centrifugal force^{17, 18} to drive the liquid through the microfluidic structures. Despite their simplicity, low cost and size, these manual pumps are limited to short-term experiments.

Active pumping of liquid, on the other hand, is generally facilitated using external, bulky pumps such as syringe, peristaltic, or pressure pumps¹⁹⁻²¹. These pumps enable a wide range of flow rates, are highly controllable, and can be used for long-term experiments. However, the cost and size of these pumps limit their utilisation to research laboratories, and even in this case a limited number of pumps can be used simultaneously. Alternative pumping mechanisms utilising automated centrifugal microfluidic platforms²²⁻²⁴ or mechanical deformation of elastic microfluidic channels²⁵ capable of performing multi-step assays have also been introduced. Miniaturised pumps taking advantage of piezoelectric actuators can replace the bulky pumps to enable portable microfluidic devices^{26, 27}. However, the cost of commercially available pumps can still be a limiting factor. The evolution of micro-fabrication techniques has also enabled the development of customised miniaturised pumps, which take advantage of various mechanical^{28, 29}, acoustic³⁰, piezoelectric^{31, 32}, electrostatic³³, electroosmotic³⁴ or pneumatic³⁵⁻³⁹ mechanisms for driving the liquid. However, the fabrication, integration and maintenance of these pumps and their reliance on external actuating and controlling components might still limit their widespread application. Liquid metal pumps made of gallium alloys can be easily fabricated and integrated by simply injecting a millimetre size droplet of liquid metal onto the desired locations of the device^{40, 41}. However, the sensitivity of these pumps to surrounding liquid and the exposure of biological samples to gallium ions⁴² might limit their suitability for biomedical applications.

In this work, we demonstrate a self-sufficient, inexpensive, and disposable active microfluidic pump, which is made of latex balloons. The versatility of the pump is demonstrated by operating various microfluidic structures, liquid viscosities, environment temperatures, and conducting long-term experiments. The flow rate can be easily controlled by varying the size and thickness of the balloon. The accessibility of the balloon pump is showcased by coupling multiple pumps to multi-inlet microfluidic systems for micro-mixing, flow focusing, and droplet generation. Importantly, the soft structure of the balloon allows for instantaneous pressure change by manual squeezing, which leads to an almost instantaneous change of flow rate through the microfluidic system. This unique feature has been utilised for dynamically changing the flow ratios of parallel streams and size of droplets. These features make the balloon pump suitable for research, educational, and *in-situ* monitoring applications.

Balloon pump setup

The balloon pump consisted of a latex balloon (25 cm helium quality balloons, Artwrap, Australia) inflated by air using a hand pump. The balloon was interfaced with a liquid prefilled syringe (5 mL, Braun, Germany) using short sections of PVC aquarium tube (ID = 4 mm, OD = 6 mm) with an optional two-way plastic air valve (Aqua One, Australia) to act as an on/off switch. The interfaces of the PVC tube with the balloon and syringe were sealed using a removable adhesive (Blu Tack, Bostic). The overall cost of the balloon pumping system is approximately US\$1 (~20 cents for a helium quality latex balloon, ~10 cents for a 10 cm PVC tube, ~50 cents for a two-way air valve, and ~20 cents for a 5 mL plastic syringe). A standard 1.5 m tailor's measuring tape (Hoechstmass®) with an accuracy of 1 mm was used to measure the circumference of inflated balloons. The process of assembling the balloon pump and coupling it to our microfluidic system is presented in **Figure S1**. More complicated fluidic interfaces can be used to enable the mounting of two or more balloons, allowing for adjusting the balloon size between the successive experiments without removing the operating balloon.

The pump was connected to the desired microfluidic structure using a 21-gauge needle (Braun, Germany) and Tygon® tubing (ID = 0.5 mm, OD = 1.5 mm, Sigma-Aldrich) (**Figure 1a**). The microfluidic devices were fabricated from polydimethylsiloxane (PDMS) using conventional lithography techniques⁴³. Inlet/outlet ports were made using a 0.75 mm biopsy punch (Harris Uni-Core). The devices were mounted on standard glass microscope slides (Thermo Scientific, L×W×H= 76×26×1 mm), and permanently bonded to glass using a plasma cleaner (Harrick Plasma, PDC-002) to avoid leakage.

To ensure the self-sufficiency of our system, we utilised a USB microscope (Digitech, 5MP USB 2.0 Digital Microscope) to monitor the flow of liquid through the microfluidic structures. A photograph of the experimental setup is presented in **Figure S2**.

Principles of the balloon pump

The pump operates as a pressure pump, in which the pressurised air inside the balloon pushes the liquid column inside the syringe, enabling it to flow through the downstream microfluidic structures. For example, coupling a balloon with a circumference of 75 cm to a 5 mL syringe prefilled with water generates a flow rate of $\sim 39 \mu\text{L}/\text{min}$ through a serpentine channel schematically shown in **Figure 1a**. The induced liquid flow rate depends on the balloon inflation pressure (the difference between the balloon internal pressure and the atmospheric pressure) and the viscous pressure drop along the microfluidic structure and interconnecting tubes, as described below:

$$P_{\text{balloon}} - P_{\infty} = \Delta P_{\text{tubes}} + \Delta P_{\text{channel}} = 2 \left(\frac{128 \mu Q L_{\text{tube}}}{\pi D_{\text{tube}}^4} \right) + \frac{k \mu Q L_{\text{channel}}}{W_{\text{channel}} H_{\text{channel}}^3} \quad (1)$$

in which P_{balloon} and P_{∞} are the internal balloon and atmospheric pressure, μ is the liquid dynamic viscosity, Q is the liquid flow rate, L_{tube} and D_{tube} are the length and internal diameter of Tygon® tube, k is a dimensionless parameter that depends on the aspect ratio of the microfluidic channel⁴⁴, while L_{channel} , W_{channel} and H_{channel} are the length, width and height of the microfluidic channel, respectively. Given that $D_{\text{tube}} \gg H_{\text{channel}}$, the majority of the pressure drop occurs along the microfluidic channel. For example, for the serpentine channel shown in **Figure 1a**, $\Delta P_{\text{channel}} \approx 9 \Delta P_{\text{tubes}}$.

We used a custom-made U-tube manometer (**Figure S3**) to measure the inflation pressure of the balloon using the $P_{\text{balloon}} - P_{\infty} = \rho g \Delta H$ equation, where ρ is the density of water, g is gravitational acceleration and ΔH is the height difference of water columns in the opposite arms of the tube. These measurements revealed the non-linear pressure-circumference (pressure-radius) curve of the balloon (**Figure 1b**). A local pressure peak was recorded at a balloon circumference of ~ 25 cm. This was followed by a plateaued pressure for balloon circumferences ranging from 45 to 60 cm. The pressure increased exponentially beyond this point. Balloon circumferences larger than 80 cm were not tested due to the risk of bursting.

The non-linear relationship between the inflation pressure and circumference (radius) of latex balloons is attributed to their hyper-elastic structure, which using the spherical thin shell model⁴⁵⁻⁴⁸ can be described as below:

$$P_{\text{balloon}} - P_{\infty} = \frac{2 \gamma t_o}{r_o} k(\lambda) (\lambda^{-1} - \lambda^{-7}) \quad (2)$$

in which, γ is the shear modulus of the latex, t_o and r_o are thickness and non-deformed radius of the balloon, respectively, $\lambda = r/r_o$ is the stretch ratio of the balloon, and $k(\lambda) = 1 + \alpha \lambda^2$ using the Mooney–Rivlin model^{49, 50} with α defined as a dimensionless

parameter. This unexpected phenomenon has been demonstrated by the famous two-balloon experiment in which a small balloon paradoxically inflates a large balloon^{51, 52}.

According to equation (2), the inflation pressure of the balloon is proportional to the thickness of the balloon shell. Taking advantage of this relationship, we doubled the inflation pressure of the balloon by simply inflating a balloon inside another similar balloon. This increased the thickness of the balloon shell from 220 to 440 μm . The pressure-circumference curve of this so-called ‘double layered balloon’ was similar to that of the single layered balloon but was multiplied by a factor of two (**Figure 1b**).

The balloon pump was then coupled to a serpentine microfluidic chip (**Figure 1a**), to measure the flow rate of water. Our experiments indicated that the flow rate curve follows exactly the trend of the pressure-circumference curve. This is not surprising as the flow rate is proportional to the internal pressure of the balloon, as described in **Equation 1**. This enabled us to obtain the characteristic curve of the balloon pump, relating the induced flow rate to the circumference and inflation pressure of the balloon, defined as $P_{\text{balloon}} - P_{\infty}$ (**Figure 1b**). Likewise, the flow rate of the ‘double layer balloon’ was twice that of the single balloon.

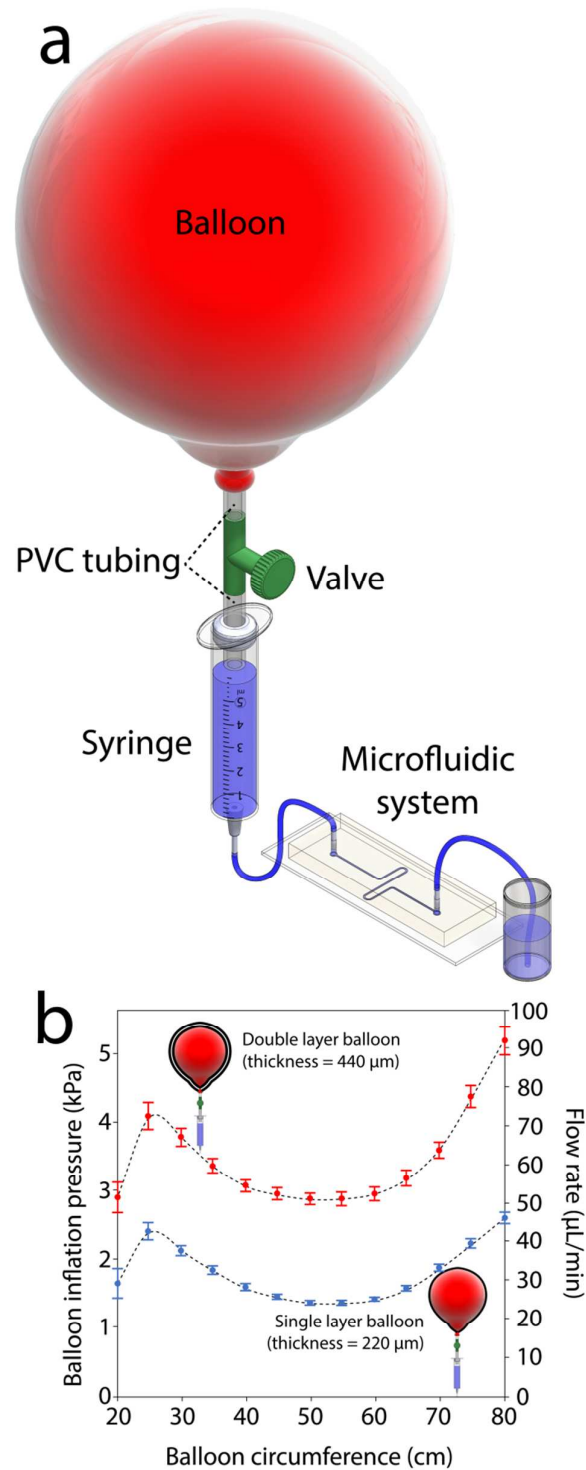


Figure 1: Balloon pump: **(a)** Schematics of the balloon pump, consisting of a latex balloon coupled to a syringe filled with liquid and then interfaced to a microfluidic chip using Tygon® tubing. **(b)** Variations of balloon inflation pressure and water flow rate through a serpentine microfluidic against the balloon circumference using both single and double layered balloons. Error bars represent average \pm STD values obtained from six sets of independent experiments.

Characterisation of the balloon pumps

We examined the performance of balloon pumps under various operating conditions. Our reference pumping system comprised of a helium quality latex balloon with a shell thickness of 220 μm inflated to a circumference of 75 cm, coupled to a 5 mL syringe, and the reference microfluidic system comprised of a straight channel ($L \times W \times H = 40 \text{ mm} \times 500 \mu\text{m} \times 80 \mu\text{m}$) interfaced with 30 cm long Tygon® tubes with an internal diameter of 0.5 mm at both inlet and outlet ports. The syringe out was kept at the level of the microfluidic chip to minimise the effect of gravity. Experiments were conducted at 23 °C. Details of the number of experiment repeats, and the mathematical equations used for fitting curves to the experimental data points obtained here are provided in **Table S1**.

Channel configuration: To examine the effect of channel configuration, we compared the flow rate of water through four microfluidic structures, including straight and serpentine channels with various numbers of turns (**Figure 2a + Figure S4**). The inertial effects at the serpentine turns were negligible due to the low flow rate of liquid, and hence the flow rate reduced inversely proportional to the channel length, as described by **Equation 1**.

Viscosity: To study the effect of liquid viscosity, we examined the flow rate using various mixtures of water and glycerol with viscosities ranging from 1 to 50 times the viscosity of water. Our experiments indicated the reduction of flow rate inversely proportional to the viscosity of the mixture (**Figure 2b**), as described by **Equation 1**. This demonstrates the versatility of the balloon pump for injecting biological liquids with various viscosities^{53, 54}.

Temperature: To demonstrate the adaptability of the balloon pump to ambient conditions, we measured the flow rate at ambient temperatures ranging from 23 to 35°C. Our experiments indicated the slight increase of flow rate against temperature (**Figure 2c**). This is due to decrease of water viscosity against temperature⁵⁵ along with decrease of balloon internal pressure as measured using our custom-made U-tube manometer, both shown as insets. The combination of these two parameters increased the flow rate of water by ~9%.

Fatigue: To examine the fatigue of the balloon pump over extended uses, we compared the flow rates over 15 successive inflations. The results showed a higher flow rate for the first two inflations, after which the flow rate stabilised. This was consistent for different balloon circumferences ranging from 55 to 75 cm (**Figure 2d**). This suggests that when using a new balloon, it should be inflated to the desired circumference at least two times before expecting consistent flow rates. Our experiments indicated that the latex balloons (especially when inflated to 75 cm or above) become susceptible to bursting after 15 successive inflations, and therefore are not recommended to be re-inflated beyond this point.

Controllability: The flow rate of the balloon pump could be reduced by simply raising the waste outlet. The reduction of flow rate was linear with respect to the height of the waste outlet (**Figure 2e**). This corresponds to the addition of the gravity pressure drop term (ρgH) to the right-hand side of **Equation 1**. This also suggests that the same pumping effects can be produced by increasing the height of the syringe to act as a gravity pump⁵⁶. As a rule of thumb, lifting a water pre-filled syringe by 10 cm corresponds to 1 kPa pressure. This enables the user to estimate the amount of height required to produce similar flow rates produced by the balloon pump (**Figure 1b**). For example, a height of 22.4 cm is required to produce similar flow rates to an inflated balloon with a circumference of 75 cm. However, the problems associated with placing the syringes at the specified heights, especially when using multiple syringes, make the balloon pump preferable.

Long-term experiments: To investigate the suitability of the balloon pump for long-term experiments, we measured the flow rate of the pump over a 12-hour period. We utilised a 30 mL syringe along with a single serpentine microfluidic channel to ensure there was sufficient liquid volume during the experiment. The outlet flow was collected in a Falcon 30 mL tube, and its weight was measured using a digital scale (OHAUS PA216, USA) at 5 s intervals (**Figure 2f**). Each curve is made of 8640 raw data points obtained over a 12-hour period. **Figure S5** presents the zoomed-in data points collected over 30, 5 and 1 min periods for more clarification.

In an ideal constant-pressure balloon, the flow rate remains constant, and therefore the displaced liquid volume will be proportional to time ($V \propto t$). However, our long-term experiments indicated a slight deviation from linearity across the *displaced liquid volume* vs. *time* curve, which can be described as $V = 50.1 \times t^{0.934}$, $R^2=0.98$ (with V in μL and t in min) for the 75 cm balloon (**Figure 2f**). This can be corresponded to continuous pressure loss of the balloon potentially due to leakage of air from the latex structure, which reduces the size of the balloons over time, as indicated in our extended experiments (**Figure S6**). Consequently, the flow rate reduced from an initial value of 43.2 to 30.4 $\mu\text{L}/\text{min}$ over 12 hours. Using the above equation, the temporal flow rate can be calculated as $Q = \partial V/\partial t = 46.81 t^{-0.066}$ (with Q in $\mu\text{L}/\text{min}$ and t in min) (**Figure 2f-inset**). Almost 70% of the total flow rate drop occurred in the two hours, resulting in an almost stable flow rate over the following 10 hours.

Interestingly, smaller balloons exhibited smaller pressure loss over time (**Figure S6**). The *displaced liquid volume* vs. *time* curve can be described as $V=34.2 \times t^{0.942}$, $R^2=0.98$ for the 65 cm balloon, and $V = 25.98 \times t^{0.976}$, $R^2=0.98$ for the 55 cm balloon. The exponent of t gets

closer to one for smaller balloons, which results in more stable flow rates over a 12-hour period, as shown in the inset. This suggests the utility of the 75 cm balloon pump for long-term experiments, which are not particularly sensitive to flow rate changes (i.e. infusing cells with cell culture media overnight), but may also show that smaller balloons made be suitable in experiments that are more sensitive to flow rate decay.

To minimise the sharp pressure losses, we recommend the balloon to be used at least 30 min after being inflated. In doing so, for a typical 30-min experiment, the flow rate reduces by 4.4, 3.9 and 1.6% for the 75, 65 and 55 cm balloons, respectively (**Figure S7**).

Balloon thickness: We also compared the pumping performance of five helium quality balloons available in Australian supermarkets. The balloon thickness was measured using a micrometer (Fowler 0-25mm Outside Metric Micrometer) providing an accuracy of 4 μm , as detailed in **Figure S8**. Our measurements indicated that the thickness of the balloons varies from 220 to 270 μm , which changes the inflation pressure (measured using the U-tube manometer) and the flow rate of the balloon pumps proportionally (**Figure S8**). This is in line with **Equation 2** and the results of double layer balloon presented in **Figure 1b**. Given this variability, the user needs to measure the thickness of the balloon to predict and compare its pumping performance with the ones reported here, which are obtained using a 220 μm thick helium quality balloon.

Balloon circumference: We also characterised the variations of flow rate against different balloon circumferences for various channel configurations (straight, serpentine with single, double, and quad turns), various syringe diameters (1, 5, 10, 20 mL syringes, Braun, Germany) as well as various balloon thicknesses (single and double balloons) (**Figure 2g**). Interestingly, all flow rate curves followed the trend described in **Figure 1b**, as follows: (i) increasing the length of the channel scaled down the flow rate curves in response to increased pressure drop consistent with the trends observed in **Figure 2a**, (ii) increasing the syringe diameter had negligible effect on the flow rate curves, and (iii) increasing the thickness of the latex scaled up the flow rate curve proportionally due to increased balloon pressure.

PVC tube length: Increasing the length of the PVC tubing that connects the balloon to the syringe to 60 cm had no measurable effect on the flow rate. This allows the user to move the balloon away from the microfluidic device or microscope stage, which is advantageous compared to gravity pumps that are sensitive to height ⁵⁶.

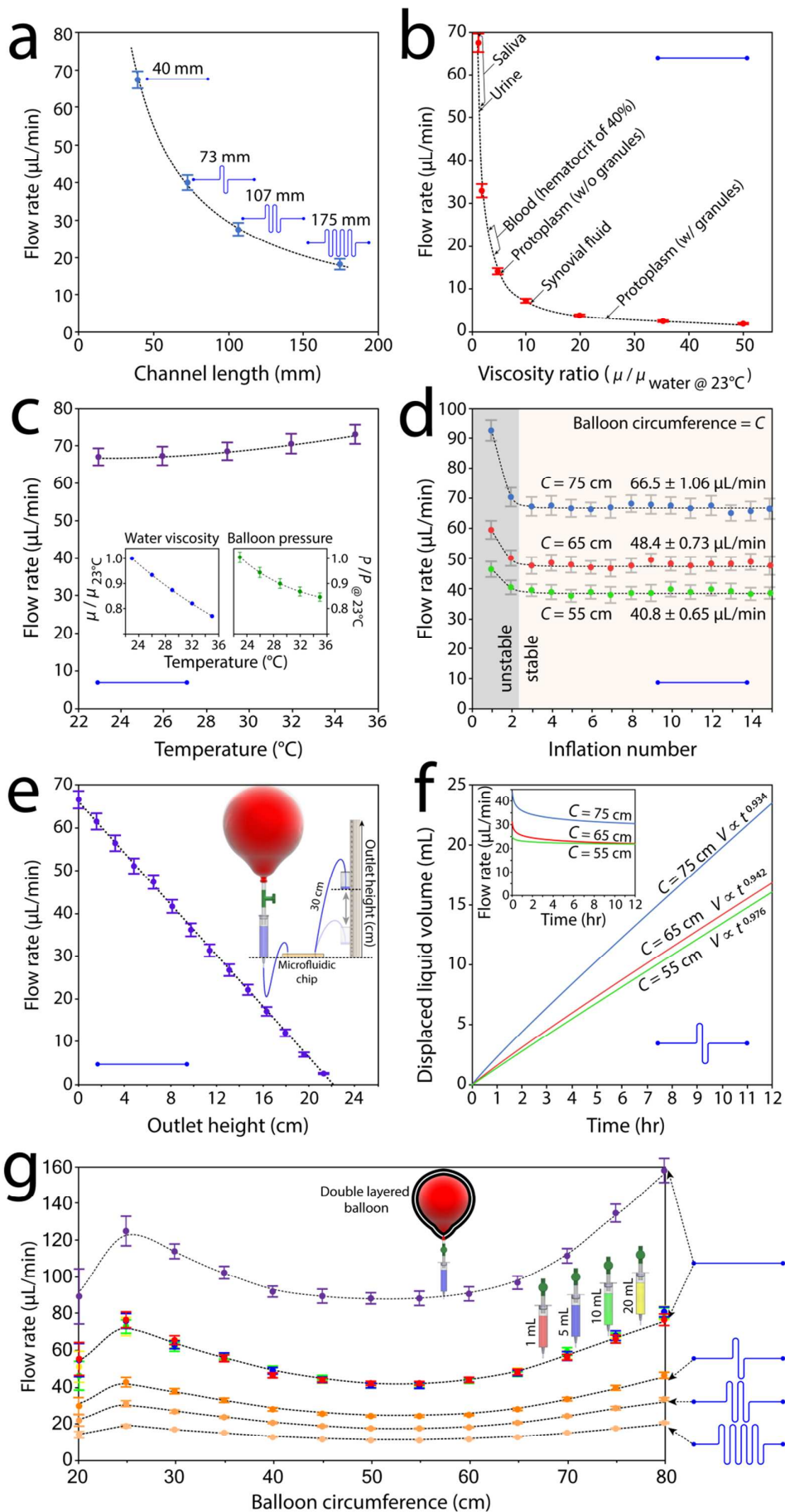


Figure 2: Characterisation of the balloon pump against influential parameters: **(a)** Channel configurations. **(b)** Liquid viscosity using various glycerol/water solutions. **(c)** Ambient temperature with insets showing the variations of water viscosity and balloon pressure versus temperature. **(d)** Fatigue of latex balloons over subsequent inflations. **(e)** Controlling the flow rate by raising the height of the outlet tube with respect to the microfluidic chip, as shown schematically in inset. **(f)** Long-term pumping, measuring the liquid volume pumped over 12 hours using three balloon circumferences with inset showing the variations of flow rate over time. **(g)** Balloon circumference tested using various microfluidic structures, syringe volumes as well as single and double balloons. See **Table S1** regarding the number of experiment repeats and the mathematical equations used for fitting curves to data points.

Passive mixing with two neighbouring flows

We conducted further experiments to investigate whether multiple balloon pumps can be used in parallel to operate more complex microfluidic setups.

We employed two balloon pumps to infuse red and blue stained water to a T-shaped microfluidic mixer (**Figure 3a**). The water was stained by adding water-based food dye (Queen) to water at a volume ratio of 1:5. Equal flow ratios were achieved by setting the circumference of both balloons to 75 cm (**Figure 3b i**). Alternatively, unequal flow ratios were obtained by creating a pressure difference between the two balloons. This was simply achieved by shrinking one of the balloons. For example, shrinking the blue balloon to 73 and 71.2 cm increased the ratio of red flow to $\varphi_{\text{red}} \sim 75\%$ and $\sim 95\%$, respectively (**Figure 3b ii-iii**). Further shrinking of the blue balloon to 70.9 cm discontinued the blue flow. **Figure 3c** shows the overlaid red flow ratios ranging from 50% to 95%. **Figure 3d** presents the variations of the red flow ratio against the circumference of the blue balloon and the inflation pressure ratio of the smaller to larger balloon: $P_{\text{blue}}/P_{\text{red}}$. The pressure ratios were obtained by our U-tube manometer setup as well as numerical simulations (**Figure S9**). Simulations were conducted by solving the differential equations governing the balance of mass, momentum and transport of multiple species transport using Fluent 6.3 software (ANSYS Inc.). Simulations were performed in 3D and under steady-state, laminar flow conditions. Our results indicated the linear variations of red flow ratio with respect to the pressure ratio of the balloons: $\varphi_{\text{red}} \propto P_{\text{blue}}/P_{\text{red}}$. This is in line with equation (1), in which the flow rate of the liquid through the microfluidic channels is proportional to the inflation pressure of the balloon.

Next, we took advantage of the elastic structure of the balloon, which enables rapid pressure changes upon manual squeezing (**Figure 3e**). In the absence of moving elements, this rapid pressure change is translated into flow rate change. This unique feature was utilised for dynamically changing the ratio of neighbouring flows in the T-shaped microfluidic mixer (**Figure 3f i-iv**). The process of squeezing and relaxing of the balloons to generate dynamic flow modes was captured using a smartphone built-in camera (iPhone 6 Plus, Apple). Still images were extracted from the recorded video at 0.1 s intervals, and analysed using ImageJ. For example, squeezing the red balloon by ~ 4 cm (~ 2 cm from each side) increased the red flow ratio from 50% to 90% within ~ 1 s. Similar dynamic patterns could be generated by laying the red balloon on the table and squeezing it by ~ 5 cm against the table. This configuration freed one hand and facilitated the manual squeezing of the red and blue balloons in repeated cycles (**Movie S1**). The smooth transition between the opposite flows

was facilitated by maintaining a short overlap between the successive squeezing cycles (i.e. start squeezing the red balloon before the blue balloon was fully relaxed). This enabled us to change the ratio of red and blue flows from $10 \pm 5\%$ to $90 \pm 5\%$ within repeated cycles of 1 ± 0.2 s with an overlap of ~ 0.15 s between the cycles, as presented in **Figure 3g** (as detailed in **Figure S10**). Our extended experiments verify the smooth transition between static and dynamic modes (**Movie S2**) as well as between successive dynamic modes with longer transition times (**Movie S3**).

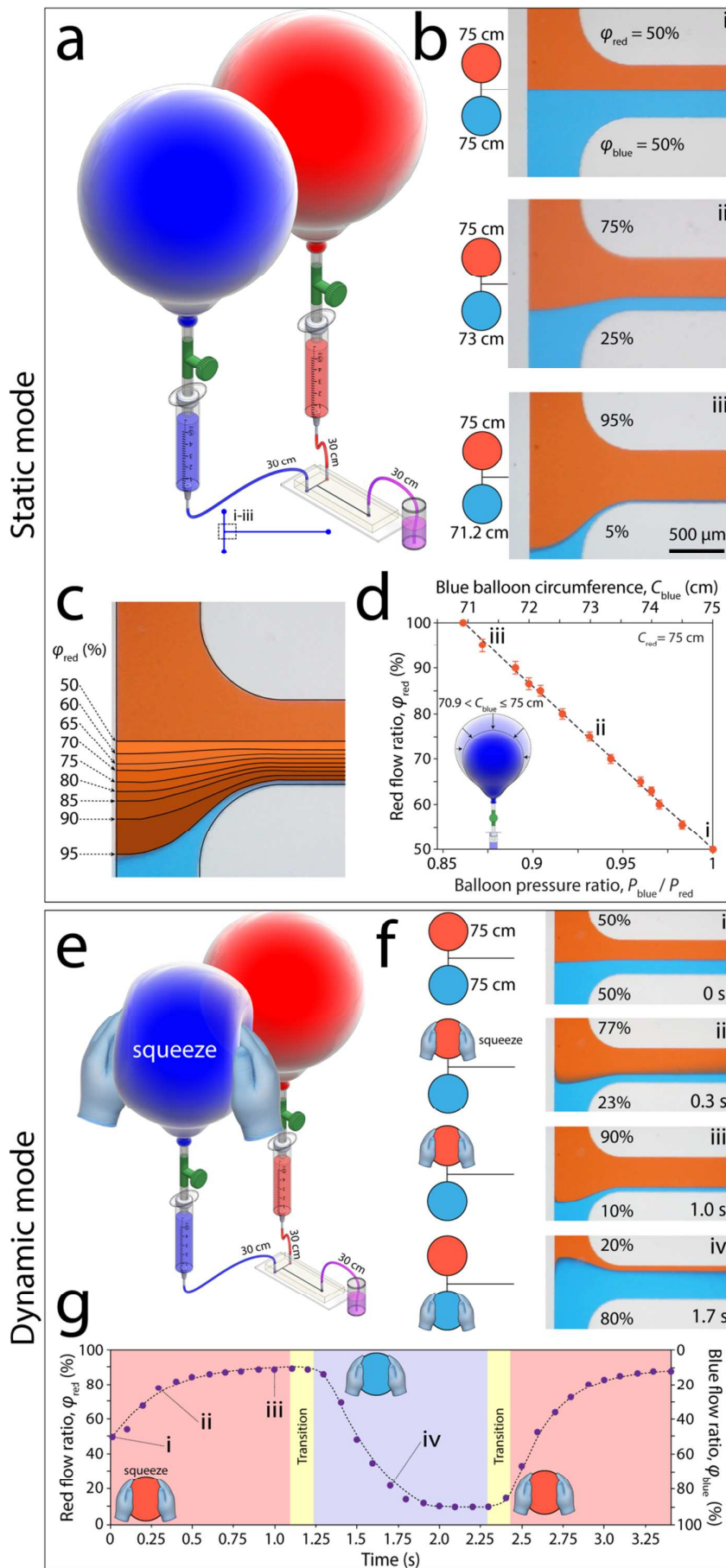


Figure 3: Operation of two balloon pumps for passive mixing of neighbouring streams in a microfluidic T-junction: **(a)** Schematic of the experimental setup. **(b)** Various flow ratios obtained under static conditions. **(c)** Overlaid red flow ratios ranging from 50% to 95%. **(d)** Variations of red flow ratio against the circumference of the blue balloon and the pressure ratio of competing balloons under static conditions. **(e)** Schematic of the experimental setup for dynamic changing of flow ratios by manual squeezing of the balloons. **(f)** Various dynamic flow ratios. **(g)** Cyclic changing of flow ratios by manual squeezing of the balloons.

Passive mixing with four neighbouring flows

To further showcase the capability of our pumping system for conducting more complex experiments, we applied four balloon pumps to infuse green, yellow, blue and red stained water simultaneously to a four-inlet microfluidic system (**Figure 4a**). Equal flow ratios were achieved by setting the circumference of upstream balloons to 75 cm while setting the circumference of downstream balloons to 68.5 cm (**Figure 4b i-iii**). The upstream balloons needed to be slightly larger to compensate the viscous pressure drop occurring prior to the second junction, as calculated by numerical simulations (**Figure S11**). Alternatively, applying four balloon pumps with the same circumference of 75 cm reduced the width of the core flows (yellow and green streams), and virtually converted the four-inlet system into a flow focusing system (**Figure 4b i'-iii'**).

We next tried to dynamically change the ratios of neighbouring flows by simply laying the balloons on the table and squeezing them, in the same fashion presented in **Movie S1**. For example, squeezing the green balloon by ~6 cm discontinued the yellow flow at the first junction and vice versa (**Figure 4c i-ii**). Likewise, simultaneous squeezing of yellow and green (upstream) balloons by ~6 cm tripled the width of yellow and green core flows at the second junction (**Figure 4c iii**). Alternatively, simultaneous squeezing of red and blue (downstream) balloons by ~6 cm discontinued the core flows, and virtually converted the four-inlet system into a T-mixer (**Figure 4c iv**). The weaker dynamic response of upstream balloons is attributed to the existence of the viscous pressure drop prior to the second junction (**Figure S11**). Upon releasing the balloons, the neighbouring flows returned to the initial mode within 2 s (**Movie S4**).

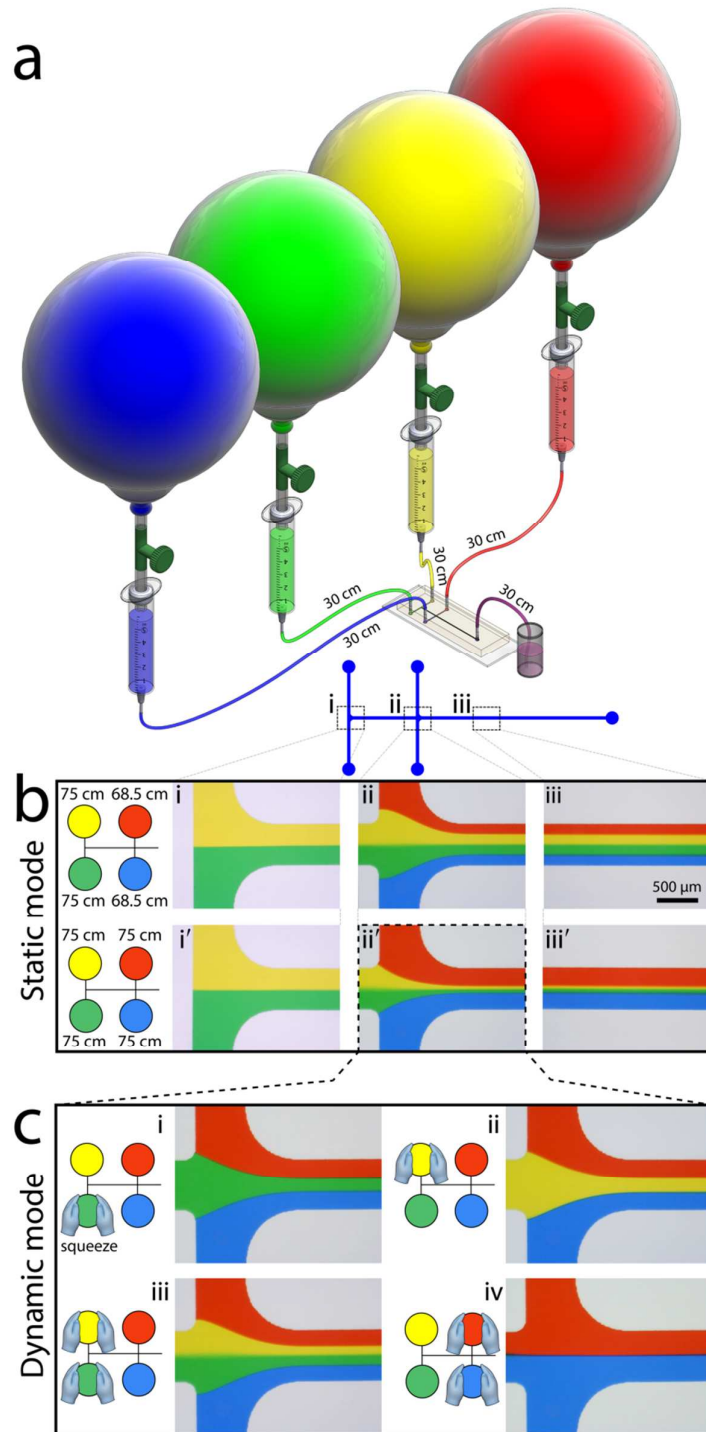


Figure 4: Operation of four balloon pumps for passive mixing and flow focusing through a four-inlet microfluidic chip: **(a)** Schematic of the experimental setup. **(b)** Various static flow ratios obtained by varying the circumference of competing balloons with insets showing balloon circumferences. **(c)** Dynamic flow ratios obtained by manually squeezing the balloons with insets showing the operational process.

Droplet generation

We also investigated the utility of our balloon pumps for droplet generation. Applying a pair of immiscible liquids such as water and oil is a well-established technique for the continuous generation of uniformly sized microscale droplets, benefiting various engineering and biological applications⁵⁷⁻⁶¹.

We employed two double layered balloon pumps to infuse blue stained water and mineral oil (RTM8, Sigma, $\mu_{\text{oil}} = 10.37$ mPa.s) through the two inlets of a flow focusing channel (**Figure 5a**). Setting the circumference of both balloons to 75 cm led to generation of water droplets with a diameter of 195 ± 8 μm at a rate of 10.5 ± 0.4 droplets/s (**Figure 5b i + Movie S5**). Shrinking the balloon at the water inlet to 72.5 and 70 cm decreased the size of droplets to 155 ± 6 and 135 ± 6 μm while decreased the rate of droplets to 4.5 ± 0.2 and 2.0 ± 0.1 droplets/s, respectively (**Figures 5b ii-iii + Movie S5**). Eventually, shrinking of this balloon to 67.5 cm discontinued the generation of water droplets, as the water did not have sufficient pressure to pass through the orifice interconnecting the flow focusing channel to the water and oil inlet channels. Our extended experiments indicated that the diameter of droplets depends on the pressure ratio of the water and oil infusing balloons, which can be described as $D_{\text{droplet}}/W_{\text{channel}} \propto (P_{\text{water}}/P_{\text{oil}})^{1.94}$ (**Figure 5c**). This is in good agreement with the findings reported by Ward et al.¹⁹, in which $D_{\text{droplet}}/W_{\text{channel}} \propto (P_{\text{water}}/P_{\text{oil}})^2$ for a pressure driven droplet generation system.

Next, we dynamically changed the size of water droplets by manually squeezing the balloons (**Figure 5d**). The circumference of the balloons at the mineral oil and water inlets was set to 75 and 67.5 cm, respectively, to ensure no water droplets are generated (**Figure 5e i**). Squeezing the water inlet balloon by ~ 4 cm (2 cm from each side) enabled the water to pass through the orifice and break into droplets. The droplets were generated with an initial size of ~ 120 μm , which is 1.6 times the width of the orifice. The droplet size increased steadily following a S-shaped (sigmoidal) curve reaching a maximum of ~ 155 μm within 1.75 s (**Figure 5e ii-iii + Movie S6**). At the same time, the generation rate of droplets increased from 2.9 ± 0.5 to 7.9 ± 0.2 droplets/s. The maximum droplet size could be maintained as long as the balloon was squeezed. Upon releasing the balloon, the water and oil flows returned smoothly to their initial mode with no water droplets generated and no backflows observed along the water or oil lines (**Movie S6**). This allowed us to dynamically change the droplet size in repeated cycles (**Figure 5f**). The variation of droplet diameter in five successive cycles is presented in **Figure S12**.

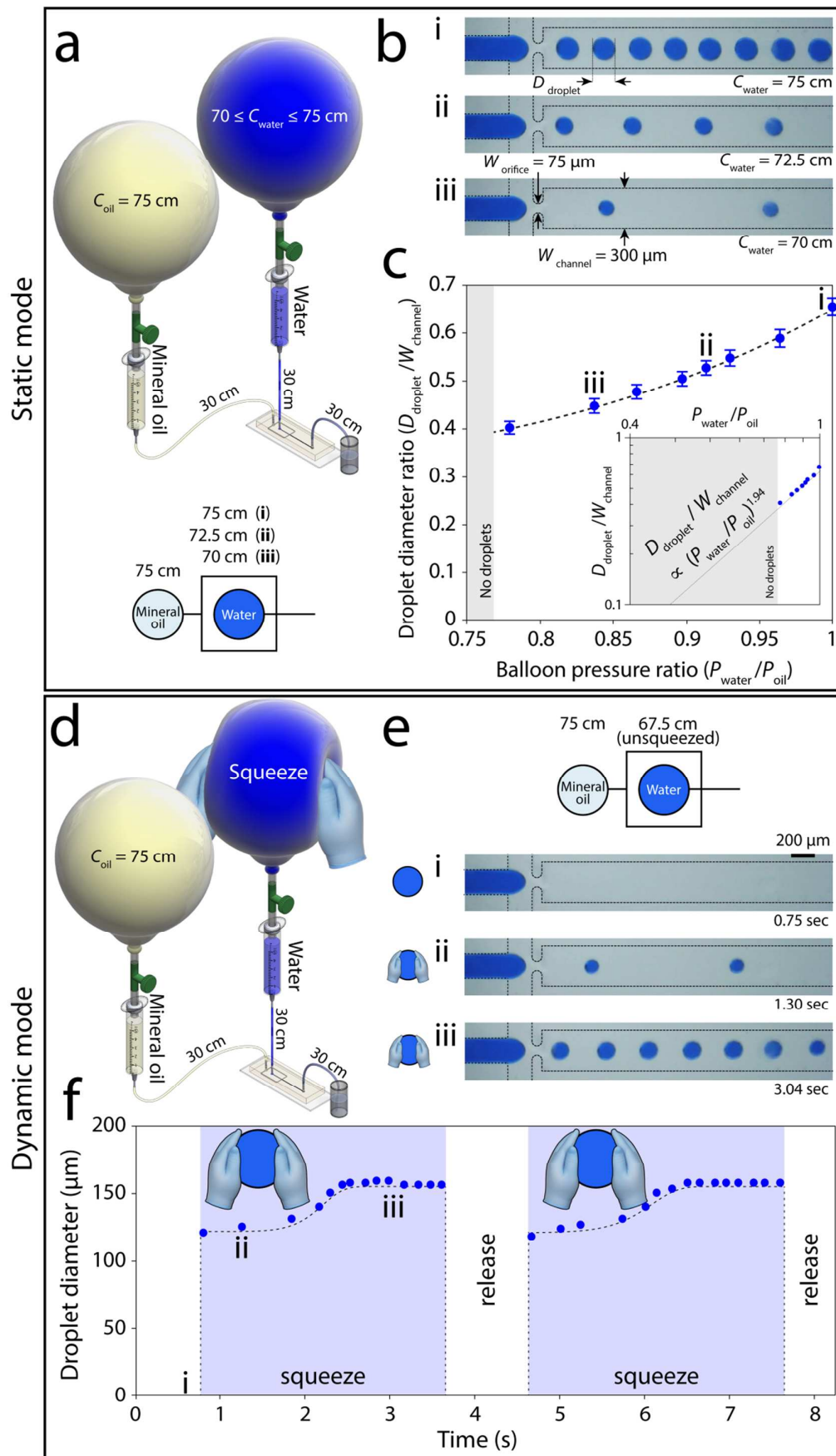


Figure 5: Microfluidic droplet generation using balloon pumps: **(a)** Schematic of the experimental setup, comprising of two balloon pumps and a microfluidic flow focusing droplet generation chip. **(b)** Decrease of droplet diameter by increasing the circumference of the balloon pump attached to water inlet under static conditions. **(c)** Variations of droplet diameter against the pressure ratio of water and oil infusing balloons. Error bars represent average \pm STD values based on 60 droplets (20 successive droplets generated in three sets of independent experiments). **(d-e)** Dynamic change of droplet diameter by squeezing the balloon pump attached to the water inlet. **(f)** Variations of droplet diameter over two successive cycles.

Conclusion

In summary, we demonstrated a self-sufficient pressure pump using commercially available latex balloons. The versatility of the balloon pump was demonstrated by driving liquid through various microfluidic structures, liquid viscosities, and ambient temperatures. The flow rate of the pump could be easily modulated by varying the size and thickness of the balloon as well as raising the waste outlet tube. Interestingly, the flow rate could be doubled using a double layered balloon. Our studies indicated the suitability of the balloon pump for conducting long-term experiments.

The accessibility and simplicity of the pump was showcased by coupling multiple balloons to multi-inlet microfluidic structures designed for passive mixing, flow focusing as well as droplet generating. In all cases, we were able to modulate the flow ratio of neighbouring flows or the size of droplets statically by coupling various balloon circumferences, and even dynamically, by manual squeezing of the balloon. The versatility of balloon pumps for varying the flow ratio of multiple parallel streams under various static and dynamic conditions make them suitable for inertial manipulation of particles and cells across neighbouring streams⁶²⁻⁶⁴, as well as for studying the response of cells following shear stress and chemical stimulation^{65,66}. Although the dynamic change of droplet size has been shown by rapidly changing the flow rate of continuous or dispersed phases via conventional pressure pumps¹⁹, changing the viscosity of continuous phase via heating⁶⁷, or changing the surface tension of disperse phase via electrowetting⁴², the simplicity of the balloon pump as well as its short response time brings new opportunities for such studies.

The self-sufficiency of the balloon pump along with its simplicity, low-cost, and versatility makes it well suited for research laboratories as well as portable *in situ* monitoring applications, and allows for conducting experiments. In addition, these features allow for running practical laboratory-based university courses as well as the promotion of science in high schools by facilitating hands-on activities in the classroom^{68,69}.

Conflict of interest: Authors declare no conflict of interest.

Acknowledgements: Authors wish to acknowledge RMIT's MicroNano Research Facility (MNRF) for fabrication of microfluidic devices. A.R.J. acknowledges the Australian National Health and Medical Research foundation Career Development Fellowship program (APP1126395). A.R.J. also acknowledges funding from the Victorian State Government

Operational Infrastructure Support and Australian Government National Health and Medical Research Council Independent Research Institute Infrastructure Support Scheme. E.P. acknowledges the Australian National Health and Medical Research Council for funding 'The Australian Centre for Electromagnetic Bioeffects Research' (NHMRC CRE APP1135076). S.B. acknowledges the Australian Research Council for Discovery for Early Career Researchers Award (DE170100239). A.R.J. and K.K. acknowledge the Australian Research Council for Discovery Grant (DP180102049).

References

1. D. J. Laser and J. G. Santiago, *Journal of Micromechanics and Microengineering*, 2004, **14**, R35.
2. A. K. Au, H. Lai, B. R. Utela and A. Folch, *Micromachines*, 2011, **2**, 179.
3. M. Boyd-Moss, S. Baratchi, M. Di Venere and K. Khoshmanesh, *Lab on a Chip*, 2016, **16**, 3177-3192.
4. M. Zimmermann, H. Schmid, P. Hunziker and E. Delamarche, *Lab on a Chip*, 2007, **7**, 119-125.
5. B. Lin, Z. Guan, Y. Song, E. Song, Z. Lu, D. Liu, Y. An, Z. Zhu, L. Zhou and C. Yang, *Lab on a Chip*, 2018, **18**, 965-970.
6. C. Szydzik, K. Khoshmanesh, A. Mitchell and C. Karnutsch, *Biomicrofluidics*, 2015, **9**, 064120.
7. T. Kokalj, Y. Park, M. Vencelj, M. Jenko and L. P. Lee, *Lab on a Chip*, 2014, **14**, 4329-4333.
8. P. Garstecki, M. J. Fuerstman, M. A. Fischbach, S. K. Sia and G. M. Whitesides, *Lab on a Chip*, 2006, **6**, 207-212.
9. K. Han, Y.-J. Yoon, Y. Shin and M. K. Park, *Lab on a Chip*, 2016, **16**, 132-141.
10. D. Bardin and A. P. Lee, *Lab on a Chip*, 2014, **14**, 3978-3986.
11. S. Smith, R. Sewart, H. Becker, P. Roux and K. Land, *Microfluidics and Nanofluidics*, 2016, **20**, 163.
12. S. Smith, P. Madzivhandila, R. Sewart, U. Govender, H. Becker, P. Roux and K. Land, *SLAS TECHNOLOGY: Translating Life Sciences Innovation*, 2017, **22**, 176-185.
13. J. Park and J.-K. Park, *Lab on a Chip*, 2018, **18**, 1215-1222.
14. K. Iwai, K. C. Shih, X. Lin, T. A. Brubaker, R. D. Sochol and L. Lin, *Lab on a Chip*, 2014, **14**, 3790-3799.
15. Y. Mukouyama, Y. Morimoto, S. Habasaki, T. Okitsu and S. Takeuchi, 2015.
16. G. Korir and M. Prakash, *PLOS ONE*, 2015, **10**, e0115993.
17. L. Zhang, F. Tian, C. Liu, Q. Feng, T. Ma, Z. Zhao, T. Li, X. Jiang and J. Sun, *Lab on a Chip*, 2018, **18**, 610-619.
18. M. S. Bhamla, B. Benson, C. Chai, G. Katsikis, A. Johri and M. Prakash, *Nature Biomedical Engineering*, 2017, **1**, 0009.
19. T. Ward, M. Faivre, M. Abkarian and H. A. Stone, *Electrophoresis*, 2005, **26**, 3716-3724.
20. T. Roy, K. Szuttor, J. Smiatek, C. Holm and S. Hardt, *Soft Matter*, 2017, **13**, 6189-6196.
21. S. Lignel, A.-V. Salsac, A. Drelich, E. Leclerc and I. Pezron, *Colloids and Surfaces A: Physicochemical and Engineering Aspects*, 2017, **531**, 164-172.
22. J. Park, V. Sunkara, T.-H. Kim, H. Hwang and Y.-K. Cho, *Analytical Chemistry*, 2012, **84**, 2133-2140.
23. M. M. Aeinehvand, F. Ibrahim, S. W. harun, W. Al-Faqheri, T. H. G. Thio, A. Kazemzadeh and M. Madou, *Lab on a Chip*, 2014, **14**, 988-997.
24. G. Wang, J. Tan, M. Tang, C. Zhang, D. Zhang, W. Ji, J. Chen, H.-P. Ho and X. Zhang, *Lab on a Chip*, 2018, **18**, 1197-1206.
25. S. B. Im, M. J. Uddin, G. J. Jin and J. S. Shim, *Lab on a Chip*, 2018, DOI: 10.1039/C8LC00003D.
26. J. Akagi, K. Khoshmanesh, C. J. Hall, J. M. Cooper, K. E. Crosier, P. S. Crosier and D. Wlodkowic, *Sensors and Actuators B: Chemical*, 2013, **189**, 11-20.
27. N. Okura, Y. Nakashoji, T. Koshirogane, M. Kondo, Y. Tanaka, K. Inoue and M. Hashimoto, *Electrophoresis*, 2017, **38**, 2666-2672.
28. J. Döpfer, M. Clemens, W. Ehrfeld, S. Jung, K. P. Kämper and H. Lehr, *Journal of Micromechanics and Microengineering*, 1997, **7**, 230.

29. L. Dong and H. Jiang, *Soft Matter*, 2007, **3**, 1223-1230.
30. M. K. Tan, L. Y. Yeo and J. R. Friend, *EPL (Europhysics Letters)*, 2009, **87**, 47003.
31. N.-T. Nguyen and T.-Q. Truong, *Sensors and Actuators B: Chemical*, 2004, **97**, 137-143.
32. P.-H. Cazorla, O. Fuchs, M. Cochet, S. Maubert, G. Le Rhun, Y. Fouillet and E. Defay, *Sensors and Actuators A: Physical*, 2016, **250**, 35-39.
33. J. Xie, J. Shih, Q. Lin, B. Yang and Y.-C. Tai, *Lab on a Chip*, 2004, **4**, 495-501.
34. S. Litster, M. E. Suss and J. G. Santiago, *Sensors and Actuators A: Physical*, 2010, **163**, 311-314.
35. M. A. Unger, H.-P. Chou, T. Thorsen, A. Scherer and S. R. Quake, *Science*, 2000, **288**, 113-116.
36. R. Gómez-Sjöberg, A. A. Leyrat, D. M. Pirone, C. S. Chen and S. R. Quake, *Analytical Chemistry*, 2007, **79**, 8557-8563.
37. Y.-S. Lee, N. Bhattacharjee and A. Folch, *Lab on a Chip*, 2018, **18**, 1207-1214.
38. P. E. Guevara-Pantoja, R. J. Jimenez-Valdes, J. L. Garcia-Cordero and G. A. Caballero-Robledo, *Lab on a Chip*, 2018, **18**, 662-669.
39. Y. Lee, D.-M. Kim, Z. Li, D.-E. Kim and S.-J. Kim, *Lab on a Chip*, 2018, **18**, 915-922.
40. S.-Y. Tang, K. Khoshmanesh, V. Sivan, P. Petersen, A. P. O'Mullane, D. Abbott, A. Mitchell and K. Kalantar-zadeh, *Proceedings of the National Academy of Sciences*, 2014, **111**, 3304-3309.
41. J. Y. Zhu, P. Thurgood, N. Nguyen, K. Ghorbani and K. Khoshmanesh, *Lab on a Chip*, 2017, **17**, 3862-3873.
42. S. Y. Tang, I. D. Joshipura, Y. Lin, K. Kalantar-Zadeh, A. Mitchell, K. Khoshmanesh and M. D. Dickey, *Advanced Materials*, 2016, **28**, 604-609.
43. D. B. Weibel, W. R. DiLuzio and G. M. Whitesides, *Nature Reviews Microbiology*, 2007, **5**, 209.
44. M. J. Fuerstman, A. Lai, M. E. Thurlow, S. S. Shevkoplyas, H. A. Stone and G. M. Whitesides, *Lab on a Chip*, 2007, **7**, 1479-1489.
45. A. Needleman, *International Journal of Solids and Structures*, 1977, **13**, 409-421.
46. I. Müller and H. Struchtrup, *Mathematics and Mechanics of Solids*, 2002, **7**, 569-577.
47. L. M. Kanner and C. O. Horgan, *International Journal of Non-Linear Mechanics*, 2007, **42**, 204-215.
48. R. Mangan and M. Destrade, *International Journal of Non-Linear Mechanics*, 2015, **68**, 52-58.
49. M. Mooney, *Journal of Applied Physics*, 1940, **11**, 582-592.
50. R. S. Rivlin, *Philosophical Transactions of the Royal Society of London. Series A, Mathematical and Physical Sciences*, 1948, **241**, 379-397.
51. D. Merritt and F. Weinhaus, *American Journal of Physics*, 1978, **46**, 976-977.
52. E. Verron and G. Marckmann, *Thin-Walled Structures*, 2003, **41**, 731-746.
53. R. S. Johnson and W. Niedermeier, *The Alabama journal of medical sciences*, 1968, **5**, 428-433.
54. H. Inoue, K. Ono, W. Masuda, T. Inagaki, M. Yokota and K. Inenaga, *Journal of Oral Biosciences*, 2008, **50**, 134-141.
55. P. M. Kampmeyer, *Journal of Applied Physics*, 1952, **23**, 99-102.
56. D. R. Albrecht and C. I. Bargmann, *Nature Methods*, 2011, **8**, 599.
57. W. Shi, J. Qin, N. Ye and B. Lin, *Lab on a Chip*, 2008, **8**, 1432-1435.
58. J.-C. Baret, O. J. Miller, V. Taly, M. Ryckelynck, A. El-Harrak, L. Frenz, C. Rick, M. L. Samuels, J. B. Hutchison, J. J. Agresti, D. R. Link, D. A. Weitz and A. D. Griffiths, *Lab on a Chip*, 2009, **9**, 1850-1858.
59. R. Zilionis, J. Nainys, A. Veres, V. Savova, D. Zemmour, A. M. Klein and L. Mazutis, *Nature Protocols*, 2016, **12**, 44.

60. B. Gol, F. J. Tovar-Lopez, M. E. Kurdzinski, S.-Y. Tang, P. Petersen, A. Mitchell and K. Khoshmanesh, *Lab on a Chip*, 2015, **15**, 2476-2485.
61. W. Wang, R. Xie, X.-J. Ju, T. Luo, L. Liu, D. A. Weitz and L.-Y. Chu, *Lab on a Chip*, 2011, **11**, 1587-1592.
62. J. S. Dudani, D. E. Go, D. R. Gossett, A. P. Tan and D. Di Carlo, *Analytical Chemistry*, 2014, **86**, 1502-1510.
63. M. Lu, A. Ozcelik, C. L. Grigsby, Y. Zhao, F. Guo, K. W. Leong and T. J. Huang, *Nano Today*, 2016, **11**, 778-792.
64. J. S. Dudani, D. R. Gossett, H. T. K. Tse, R. J. Lamm, R. P. Kulkarni and D. D. Carlo, *Biomicrofluidics*, 2015, **9**, 014112.
65. S. Baratchi, F. J. Tovar-Lopez, K. Khoshmanesh, M. S. Grace, W. Darby, J. Almazi, A. Mitchell and P. McIntyre, *Biomicrofluidics*, 2014, **8**, 044117.
66. S. Baratchi, M. Knoerzer, K. Khoshmanesh, A. Mitchell and P. McIntyre, *Scientific Reports*, 2017, **7**, 15942.
67. C. A. Stan, S. K. Y. Tang and G. M. Whitesides, *Analytical Chemistry*, 2009, **81**, 2399-2402.
68. D. Nguyen, J. McLane, V. Lew, J. Pegan and M. Khine, *Biomicrofluidics*, 2011, **5**, 022209.
69. N. J. Cira, A. M. Chung, A. K. Denisin, S. Rensi, G. N. Sanchez, S. R. Quake and I. H. Riedel-Kruse, *PLOS Biology*, 2015, **13**, e1002110.